Guard Beams

Coverage Enhancement of UE-Centered ISAC via Analog Multi-Beamforming

Hersyandika, Rizqi; Sakhnini, Adham; Miao, Yang; Wang, Qing; Pollin, Sofie

DOI
10.1109/ACCESS.2024.3491939

Publication date
2024

Document Version
Final published version

Published in
IEEE Access

IEEE Access
Multidisciplinary ⋮ Rapid Review ⋮ Open Access Journal

Received 9 September 2024, accepted 29 October 2024, date of publication 5 November 2024, date of current version 13 November 2024.

Digital Object Identifier 10.1109/ACCESS.2024.3491939

RESEARCH ARTICLE

Guard Beams: Coverage Enhancement of UE-Centered ISAC via Analog Multi-Beamforming

RIZQI HERSYANDIKA[1], (Graduate Student Member, IEEE), ADHAM SAKHNINI[1,2], (Student Member, IEEE), YANG MIAO[1,3], (Senior Member, IEEE), QING WANG[4], (Senior Member, IEEE), AND SOFIE POLLIN[1,2], (Senior Member, IEEE)

[1]Department of Electrical Engineering, KU Leuven, 3001 Leuven, Belgium
[2]Interuniversity Microelectronics Centre (IMEC), 3001 Leuven, Belgium
[3]Department of Electrical Engineering, University of Twente, 7522 NB Enschede, The Netherlands
[4]Department of Software Technology, Delft University of Technology, 2628 CD Delft, The Netherlands

Corresponding author: Rizqi Hersyandika (rizqi.hersyandika@kuleuven.be)

This work has received funding from the European Union's Research and Innovation Program under Grant 861222 - Millimeter-wave Networking and Sensing for Beyond 5G (MINTS Project) and Grant 101096954 - Building Reusable Testbed Infrastructures for Cloud-to-Device Breakthrough Technologies (6G-BRICKS Project).

ABSTRACT This paper introduces an Integrated Sensing and Communication (ISAC) approach to safeguard communication User Equipment (UE) from approaching objects or people, such as potential blockers, without the need to scan the entire environment, while providing continuous communication services. The proposed UE-centered ISAC system utilizes a communication-centric waveform, transmitted through *guard beams* to monitor the area within the UE proximity. These guard beams are generated through a multi-beamforming technique employing a shared analog array that also generates the communication beam. The parameters for generating the guard beams are optimized to maximize sensing coverage while adhering to the communication Signal-to-Noise Ratio (SNR) constraints. In comparison to the detection using the communication-beam-only system, our optimized guard beams enhance the detection range and coverage area by over 1.5 times while maintaining the required communication SNR. Our multi-stage sensing pipeline applied to the guard beams significantly reduces the complexity of sensing signal processing required to detect approaching blockers while maintaining accuracy comparable to that of exhaustive scanning based on the grid-searching method. Furthermore, the guard beams approach reduces the impact on communication SNR by 0.7 dB factor compared to exhaustive scanning with a balanced communication-sensing power allocation, offering a less pronounced impact on the communication performance in an ISAC system.

INDEX TERMS Beam resource allocation, integrated sensing and communication, millimeter-Wave, mono-static sensing, multi-beamforming.

I. INTRODUCTION

A. MOTIVATION

Millimeter-Wave (mmWave) communication has been considered as a key enabler of 5G-and-beyond wireless networks due to its potential to achieve multi-Gbps throughput, facilitated by the large bandwidth [1]. Nevertheless, relying on directional beams to compensate for the significant free-space propagation loss makes mmWave links vulnerable to blockages such as moving objects or humans, resulting in subsequent signal attenuation and performance degradation. Human activities in proximity to User Equipment (UE) can significantly impact the mmWave communication performance. A human crossing a mmWave link can create

The associate editor coordinating the review of this manuscript and approving it for publication was Wei Wang.

shadowing lasting several hundred milliseconds [2], [3]. The power attenuation induced by the human body, including scattering [4] and absorption, can reach up to 34 dB [5]. Therefore, proactive detection of potential blockages before they cast shadows over mmWave communication links is essential. Subsequent countermeasures can then be activated to maintain communication performance, such as re-steering the communication beam to alternative paths or establishing a new connection with another Base Station (BS). This is where Integrated Sensing and Communication (ISAC) can play a role in maintaining communication performance by proactively sensing the environment to identify potential link blockages.

ISAC, a key feature envisioned in 6G networks, enables simultaneous sensing services while delivering communication to the user. By harnessing shared radio frequency spectrum, waveform, and hardware resources for both functionalities, ISAC enhances the efficiency of resource utilization [6], [7]. Several ISAC use cases involve detecting human presence and sensing the surrounding environment [8]. In the context of the blockage-aware system, ISAC can be utilized to actively sense the surrounding environment to detect the presence of potential blockers, providing an anticipatory step in avoiding link blockages. Surveillance and proximity detection are important in addressing safety concerns within the factory and mining environments [9], [10]. In addition, ambient radio frequency signals from the environment can be utilized for spectrum sensing [11] and presence detection [12].

To facilitate simultaneous communication and sensing via analog beamforming, the use of multi-beams jointly designed for communication and sensing, and generated using phased array systems has been proposed in [13], [14], and [15]. This shared phase array system, i.e., shared for both communication and sensing functions, enables the dynamic generation of multiple beams tailored for communication and sensing purposes. This adaptability is achieved through beamforming weight vector adjustment of each element via the analog beamformer. The communication-centric waveform, such as Orthogonal Frequency-Division Multiplexing (OFDM) or single carrier waveform, can be leveraged to ensure communication performance while enabling the extraction of echoed information from targets for sensing purposes [16].

A notable challenge in generating multi-beams for communication and sensing using a shared phase array lies in beam resource allocation. There is a trade-off between communication and sensing performance, given that both functions share the same total power and antenna degrees of freedom. An efficient beam resource allocation strategy contributes to enhancing the overall communication and sensing performance. This problem leads us to investigate an efficient sensing strategy employing a simple joint analog multi-beam where the scanning is focused around the communication UE it protects.

B. RELATED WORKS

Numerous human blockage prediction methods in mmWave communications incorporate cameras [17], [18], [19], [20], radars [21], LiDARs [22], and sub-6 GHz channel behaviors [23], [24]. While effective, these approaches have the drawback of relying on external sensors, increasing the cost and system-level complexity of the communication system. Furthermore, devices such as cameras may raise privacy concerns. A human blockage prediction approach using an

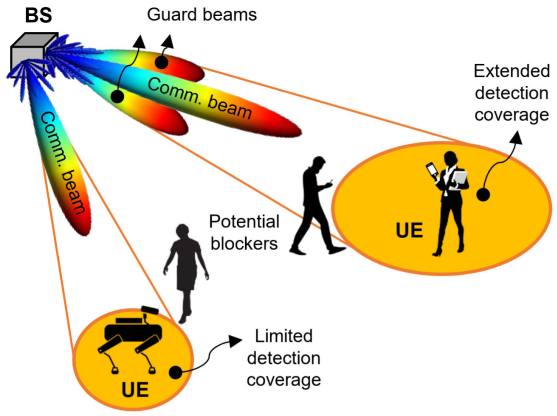

FIGURE 1. Sensing around the UE using guard beams.

in-band mmWave beam is proposed in [25] to address these challenges. The method utilizes fluctuation in the received signal strength occurring before the shadowing event to predict the future instance of a blockage. In this study, the author relies on the mmWave communication beam to detect incoming blockers in a bistatic scenario. Nevertheless, it is important to note that the field of view of this communication beam is limited, given that the mmWave base station typically transmits a narrow and highly-directional beam towards the user.

In our earlier study [26], we employ an extra beam, steered at a specific angle away from the communication beam, to broaden the detection area in a bistatic scenario. This extra beam is generated using an additional Radio Frequency (RF) chain and array. Detection is performed by observing the received signal level fluctuation caused by the constructive and destructive interferences from reflected signals when the potential blocker approaches the mmWave links. Through experimental evaluation, we demonstrate that early detection of potential blockers is achievable with the additional beam, improving the blockage detection performance obtained solely through reliance on the communication beamwidth.

Leveraging multi-beams with analog arrays for communication and sensing purposes has been studied in [13], [14], [27], [28], [29], and [30]. The works of [27] and [28] optimize the beamforming weight vector with consideration of beam quantization to generate the multi-beam, while [29] and [30] focus on suppressing the reception in the communication directions and cancelling full-duplexing

related self-interference. Nevertheless, the existing literature typically adopts a narrow sensing beam that undergoes exhaustive sweeping across the sensing field of view to detect and localize human movement in the environment. The exhaustive scanning approach incurs significant overhead, as beam scanning has to be executed multiple times to cover the sensing field of view, particularly when dealing with expansive coverage areas.

C. CONTRIBUTIONS

We present a UE-centered ISAC approach to safeguard the communication user from approaching objects or people potentially blocking the mmWave communication link by utilizing *guard beams*. The term refers to the set of beams that illuminate the area surrounding the communication UE to locate the potential blockers. Fig. 1 illustrates how the guard beams illuminate the area around the UE, extending the detection coverage to detect and localize the approaching potential blockers compared to the detection solely by communication beam. The detailed contributions of this paper are summarized as follows:

- **Guard beams:** We introduce the concept of analog-multi-beamforming-based *guard beams*, efficient sensing beams steered in directions surrounding the communication beam, generated by an analog beamformer using a shared phased array. Compared to the *guard beam* proposed in our prior work [26], which requires an additional RF chain and phased array to steer a sensing beam independently, here we utilize the same RF chain and phased array to perform both communication and sensing functionalities. It allows the BS to reuse the communication waveform to illuminate the area around the communication UE, expanding the sensing coverage beyond the directive communication beam. Notably, this approach eliminates the need to scan the entire environment to search for potential blockers.
- **Optimized multi-beam design:** We provide comprehensive design guidelines for generating the communication beam and guard beams through analog multi-beamforming technique. The steering direction of guard beams dynamically changes based on the UE position. The beamforming design involves selecting optimal steering angles of guard beams and sensing power allocation coefficients as function of UE position relative to the BS array, with the goal of maximizing the sensing coverage area around the UE while maintaining the required communication performance.
- **Multi-stage sensing pipeline:** We propose a multi-stage blocker detection and estimation strategy to accurately determine a potential blocker's range, velocity, and direction of arrival (DoA), with the key principle of utilizing different number of symbols for each stage. By dividing the sensing signal processing into multiple stages, the symbol resources can be utilized more efficiently (i.e., the Doppler estimation requiring a large number of symbols is only conducted upon target detection that requires fewer symbols). Subsequently, narrow beams are swept to refine the DoA estimation. Our proposed dynamic scan model for DoA estimation, which is based on the range information obtained in the detection stage, achieves DoA estimation accuracy comparable to the upper-bound fixed scan despite employing fewer scans.

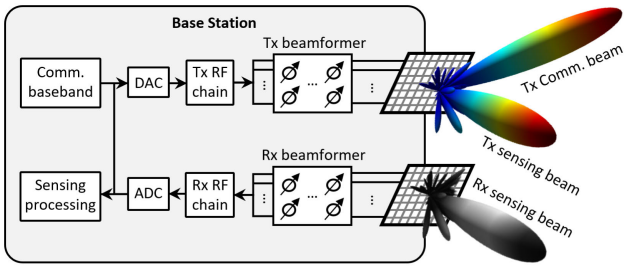

FIGURE 2. System architecture of ISAC-enabled BS employing multi-beam based on analog beamforming.

- **Enhanced sensing coverage and reduced sensing complexity:** We assess the sensing performance of guard beams, considering detection range, sensing coverage, and accuracy in sensing parameters estimation. Our findings demonstrate that guard beams extend the sensing coverage by over 1.5 times beyond the capabilities of a communication beam alone in detecting approaching blockers. In addition, guard beams facilitate DoA estimation, which is not possible with the communication-beam-only. Moreover, the guard beams approach achieves comparable accuracy in sensing parameters estimation while reducing the complexity of sensing signal processing, utilizing up to 13.83% fewer symbols compared to the exhaustive scanning method. This improvement is due to our multi-stage sensing pipeline applied to the guard beams.
- **Reduced impact on communication:** We evaluate the impact of guard beams on communication performance, including the multi-path interference resulting from additional illumination of the guard beams, and the inherent communication gain reduction as both sensing and communication share the same array. Our findings show a 0.7 dB improvement in Signal-to-Noise Ratio (SNR) compared to exhaustive scanning with a balanced communication-sensing power allocation, suggesting that the impact of guard beams on reducing communication SNR is less pronounced than with the exhaustive scanning approach.

II. SYSTEM MODEL

A. ISAC SYSTEM ARCHITECTURE

The system architecture of the ISAC-enabled BS is depicted in Fig. 2. The BS adopts a monostatic configuration with transmit (Tx) multi-beam capability. It employs a single Tx RF chain connected to an analog Uniform Planar Array

(UPA) capable of generating multi-directional Tx beams by adjusting the phase and amplitude of the analog beamformer. These beams include a Tx communication beam steered towards the served UE and a set of Tx sensing beams that illuminates the region around the UE. As a single Tx front-end is used, the same waveform simultaneously serves communication and sensing purposes. The BS system architecture could be extended with additional Tx RF chains, beamformers, and arrays to serve multiple users via hybrid MIMO. However, our study narrows its focus to a singular user scenario, delving into a more detailed mechanism to protect a UE from potential approaching blockers by employing sensing (guard) beams generated alongside the communication beam.

We assume the BS is aware of the UE's location relative to itself, as the localization of an active user is one of the 5G service requirements defined by 3GPP [31]. Periodic beam-sweeping can be employed to determine the UE's relative position, i.e., azimuth and elevation, with respect to the BS [32]. The Tx beamformer steers the Tx communication beam towards the UE direction and the Tx sensing beams around the communication beam. Since the Tx communication and sensing beams share the same antenna arrays and power budget, the beamforming weight vector for both communication and sensing will affect each other. An analog receiving (Rx) UPA connected to an Rx RF chain is utilized to receive back-scattered signals from potential blockers. The steering direction of the Rx sensing beams is aligned with the Tx sensing beams, maximizing the combined Tx–Rx gain in the intended sensing directions. Further detailed beamforming design for both Tx and Rx beamformers is presented in Section III-A.

The analog signal is converted to a baseband signal using an Analog-to-Digital Converter (ADC) for subsequent sensing processing. It is worth noting that the monostatic radar architecture causes self-interference due to Tx–Rx coupling. However, as addressing self-interference is not the primary focus of this work, we assume that state-of-the-art self-interference cancellation in both analog and digital domains (e.g., as presented in [33]) can effectively address this issue. Additionally, an approach to mitigate the interference in multi-beam communication and sensing using analog arrays has been proposed in [30].

B. ISAC WAVEFORM AND CHANNEL MODELS

We adopt a communication-centric waveform to serve both communication and sensing purposes. Specifically, we consider the 5G-NR Time Division Duplex (TDD)-based OFDM waveform [34] operating at the frequency carrier f_c with the bandwidth B. The OFDM waveform consists of K subcarriers with the subcarrier spacing denoted as Δf. The symbol period is denoted as T_p.

The BS transmits a directional Tx ISAC communication-centric beam towards a UE, generated via the Tx beamformer, and the UE generates the Rx beam towards the direction of BS to receive the signals. We consider a deterministic multipath channel model that accounts for the dominant Line-of-Sight (LoS) path and specular reflections from the moving sensing target. The received downlink signal of the k-th subcarrier and l-th symbol at the UE resulting from multi-path P can be expressed as follows:

$$y_u(k,l) = \sqrt{p_t}\, s(k,l) \sum_{p=0}^{P-1} \alpha_p e^{-j2\pi \frac{(f_0 + k\Delta f) d_p}{c}} + z_u(k,l), \quad (1)$$

where p_t is the BS transmit power, $s(k,l)$ represents the transmitted signal, α_p denotes the channel coefficient of the p-th path, f_0 is the center frequency of the first subcarrier, d_p is the p-th path distance between BS and UE, c is the speed of light, and $z_u(k,l)$ represents the additive white Gaussian noise at the UE. The p-th path gain $\beta_p = |\alpha_p|^2$ can be expressed as:

$$\beta_p = g_p^{\text{tx}} g_p^{\text{rx}} \rho_p \left(\frac{\lambda}{4\pi d_p} \right)^2, \quad (2)$$

where g_p^{tx} and g_p^{rx} represent the BS Tx beamforming gain and the UE Rx beamforming gain in the path p direction, ρ_p denotes the scattering coefficient of the path p, and $\lambda = c/f_c$ indicates the wavelength. Assuming no interference from other downlink transmissions, the downlink SNR is calculated as:

$$\chi_u = \frac{p_t \left| \sum_{p=0}^{P-1} \alpha_p e^{-j2\pi f_c d_p / c} \right|^2}{\sigma_u^2}, \quad (3)$$

where σ_u^2 represents the noise power and is formulated as $\sigma_u^2 = k\,T\,B F_u$, with k being the Boltzmann constant, T denoting the temperature, B representing the system bandwidth and F_u being the noise figure of the UE.

The BS's Rx RF chain captures the Channel State Information (CSI), which contains the backscattered signals from the target, i.e., the potential blocker. The received backscattered signal of the k-th subcarrier and l-th symbol from all targets Q at the Rx of BS after dividing with $s(k,l)$ is formulated as:

$$y_s(k,l) = \sum_{q=0}^{Q-1} \alpha_q e^{j2\pi T_p f_q l} e^{-j2\pi \frac{\Delta f d_q}{c} k} + z_s(k,l), \quad (4)$$

where α_q denotes the complex amplitude of the backscattered signal from target q, T_p is the symbol period, f_q denotes the Doppler frequency, d_q is the distance between the BS and target q, and $z_s(k,l)$ represents the additive noise. The Doppler shift can be expressed as $f_q = 2\, v_q f_c / c$, where v_q is the radial velocity of target q. The power of the q-th return $\beta_q = |\alpha_q|^2$ is expressed by:

$$\beta_q = \frac{p_t g_q^{\text{tx}} g_q^{\text{rx}} \lambda^2 \rho_q}{(4\pi)^3 d_q^4}, \quad (5)$$

where ρ_q is the Radar Cross Section (RCS), d_q represents the distance between BS and target, g_q^{tx} and g_q^{rx} denote the Tx and Rx beamforming gain of BS in the sensing direction, respectively. Assuming there is no uplink interference from

other UEs, the sensing SNR of the backscattered signal from the q-th target is expressed as:

$$\chi_q = \frac{\beta_q}{\sigma_r^2}, \tag{6}$$

where $\sigma_r^2 = k\,TBF_r$ denotes the noise at the radar receiver with F_r being the noise figure of BS receiver. The sensing signal processing is further detailed in Section IV.

C. MULTI-BEAMFORMING USING UPA

For an UPA with size of $M \times N$ antenna elements, the steering vector of the m-th horizontal element and n-th vertical element for the azimuth angle θ and the elevation angle ϕ can be respectively expressed as:

$$\hat{v}_m(\theta, \phi) = e^{-j\frac{2\pi}{\lambda} m d_x \sin\theta \cos\phi}, \tag{7}$$

$$\hat{v}_n(\theta, \phi) = e^{-j\frac{2\pi}{\lambda} n d_y \sin\theta \sin\phi}. \tag{8}$$

The steering vector of the (m, n)-th element of UPA$_{(M\times N)}$ is [35]:

$$\hat{v}_{m,n}(\theta, \phi) = \hat{v}_m(\theta, \phi)\, \hat{v}_n(\theta, \phi), \tag{9}$$

where $m = \{0, \ldots, M-1\}$ and $n = \{0, \ldots, N-1\}$. By considering a half-wavelength spacing between two horizontal elements d_x and vertical elements d_y, the steering vector becomes:

$$\hat{v}_{m,n}(\theta, \phi) = e^{-j\pi \sin\theta(m\cos\phi + n\sin\phi)}. \tag{10}$$

The overall array steering vector is denoted as $\hat{\mathcal{V}} \in \mathbb{C}^{1\times MN}$, where $\hat{\mathcal{V}} = \{\hat{v}_{1,1}, \ldots, \hat{v}_{M,N}\}$.

To steer the beam towards an intended direction, a beamforming weight vector needs to be assigned to each element. The weight vector of the (m, n)-th element for steering the beam in the direction (θ_d, ϕ_d) can be defined as follows:

$$\hat{w}_{m,n}(\theta_d, \phi_d) = e^{j\pi \sin\theta_d(m\cos\phi_d + n\sin\phi_d)}. \tag{11}$$

The beamforming weight vector of an array is denoted as $\hat{\mathcal{W}} \in \mathbb{C}^{1\times MN}$, where $\hat{\mathcal{W}} = \{\hat{w}_{1,1}, \ldots, \hat{w}_{M,N}\}$. The beamforming gain at the direction (θ, ϕ) for a given beamforming direction (θ_d, ϕ_d) can be expressed as:

$$g(\theta, \phi) = \left|\hat{\mathcal{W}}^{\mathrm{T}}(\theta_d, \phi_d)\hat{\mathcal{V}}(\theta, \phi)\right|^2. \tag{12}$$

Multiple beams can be formed simultaneously by coherently combining multiple weight vectors of communication and sensing beams [14], [28]. The Tx beamformer assigns a combined weight vector to each antenna element within the Tx UPA, formulated as:

$$\hat{\mathcal{W}}^{\mathrm{tx}} = \sqrt{(1-\eta)}\, \hat{\mathcal{W}}_c(\theta_c, \phi_c) + \sqrt{\eta}\, \hat{\mathcal{W}}_s(\theta_s, \phi_s), \tag{13}$$

where $\hat{\mathcal{W}}_c$ denotes the weight vector of the communication beam steered at (θ_c, ϕ_c) and $\hat{\mathcal{W}}_s$ represents the weight vector of the sensing beam steered at (θ_s, ϕ_s). Meanwhile, η represents the power allocation coefficient to adjust the portion of gain allocated for communication and sensing beams. The normalized Tx beamforming weight vector is obtained through $\frac{\hat{\mathcal{W}}^{\mathrm{tx}}}{|\hat{\mathcal{W}}^{\mathrm{tx}}|}$.

The communication beam is steered in the direction of UE (θ_c, ϕ_c), established through a prior beam training process between the BS and the UE, while the sensing beam is steered in the intended sensing direction (θ_s, ϕ_s). On the Rx side, the Rx beamformer of the BS assigns the following weight vector:

$$\hat{\mathcal{W}}^{\mathrm{rx}} = \hat{\mathcal{W}}_s(\theta_s, \phi_s), \tag{14}$$

focusing the Rx beam towards the same direction as the Tx sensing beam. The transmit and receive beamforming gain, g^{tx} and g^{rx}, are obtained by substituting (13) and (14) to (12). The combined Tx–Rx gain in the (θ, ϕ) direction then becomes:

$$g^{\mathrm{comb}}(\theta, \phi) = g^{\mathrm{tx}}(\theta, \phi) g^{\mathrm{rx}}(\theta, \phi). \tag{15}$$

Note that the narrowband beamforming assumption is valid thanks to a sufficiently small fraction bandwidth $\left(\frac{B}{f_c}\right)$, making the phase shift variation across different subcarriers negligible [28], [36].

III. PROPOSED GUARD BEAMS

Guard beams are composed of collective sensing beams steered at certain angles away from the communication beam to illuminate the potential blocking area around the communication user. These beams create virtual barriers that are capable of detecting the presence and localizing the moving potential blockers upon entry. The guard beams approach eliminates the need for exhaustive target search, thereby making the detection faster and simplifying the sensing signal processing compared to the grid-searching method.

A. GENERATING THE GUARD BEAMS

Unlike the grid-searching approach, where the Tx sensing beam is determined by the pre-defined codebook and is independently steered from the Tx communication beam, the steering direction of guard beams depends on the Tx communication beam direction. Two sets of guard beams, each containing N_G sub-beams, are steered to scan the potential blockers in two directions: the left and the right sides of the UE. The user-defined parameter N_G must be an odd number greater than three, ensuring a contiguous beamforming gain within the targeted area. Each sub-beam is steered in different directions around the communication beam, maintaining an identical separation angle δ away from the communication beam. Notably, one sub-beam must be steered at the same elevation as the communication beam, providing sensing coverage in either the left or the right direction. The angular space of the guard beams on each side is divided equally as follows:

$$\psi = \frac{180^\circ}{N_G - 1}. \tag{16}$$

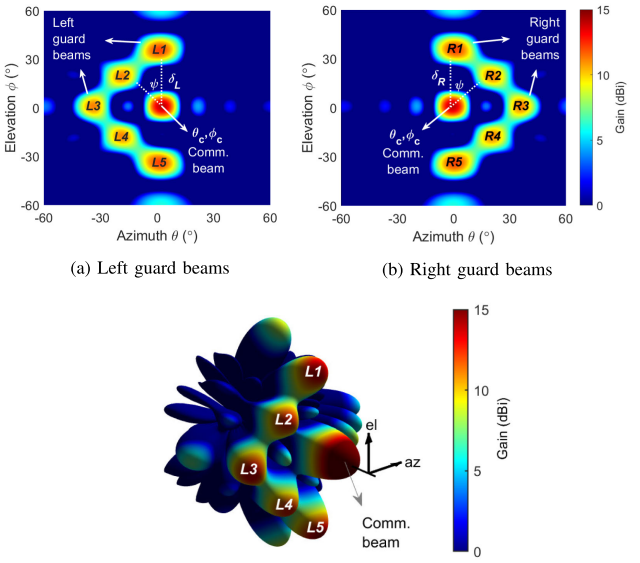

(a) Left guard beams

(b) Right guard beams

(c) Guard beams in 3D plane (the left guard beams)

FIGURE 3. Generating the Tx guard beams with $N_G = 5$ beams.

The steering angle of individual sub-beams depends on the θ_c, ϕ_c, δ and ψ. The n-th sub-beam of the left guard beams is steered in the following direction:

$$\begin{aligned} \theta_{Ln} &= \theta_c - \delta_L \sin(n\psi), \\ \phi_{Ln} &= \phi_c + \delta_L \cos(n\psi), \end{aligned} \tag{17}$$

while the n-th sub-beam of the right guard beams is steered in:

$$\begin{aligned} \theta_{Rn} &= \theta_c + \delta_R \sin(n\,\psi), \\ \phi_{Rn} &= \phi_c + \delta_R \cos(n\,\psi), \end{aligned} \tag{18}$$

where $n = \{0, 1, \ldots, N_G - 1\}$. Therefore, the beamforming weight vectors of individual sub-beams of the left and right guard beams can be formulated as the $(\theta_c, \phi_c, \delta)$–dependent function, as follows:

$$\hat{\mathcal{W}}_{Ln}(\theta_c, \phi_c, \delta_L) = \hat{\mathcal{W}}\left(\theta_c - \delta_L \sin(n\psi), \phi_c + \delta_L \cos(n\psi)\right) \tag{19}$$

$$\hat{\mathcal{W}}_{Rn}(\theta_c, \phi_c, \delta_R) = \hat{\mathcal{W}}\left(\theta_c + \delta_R \sin(n\psi), \phi_c + \delta_R \cos(n\psi)\right). \tag{20}$$

Fig. 3 illustrates the generation of both left and right guard beams. The communication beam steered at (θ_c, ϕ_c) becomes the center point, surrounded by $N_G = 5$ sub-beams, each positioned at a separation angle of δ from the communication beam. In this example, we use $\delta_L = \delta_R = 30°$ to show a clear separation between the sub-beams.

In general, the normalized beamforming weight vector of each guard beams side is obtained by combining the weight vectors of all sub-beams, expressed as:

$$\hat{\mathcal{W}}_{\text{guard}}(\theta_c, \phi_c, \delta) = \frac{\sum_{n=0}^{N_G-1} \hat{\mathcal{W}}_n(\theta_c, \phi_c, \delta)}{\left|\sum_{n=0}^{N_G-1} \hat{\mathcal{W}}_n(\theta_c, \phi_c, \delta)\right|}. \tag{21}$$

Substituting $\hat{\mathcal{W}}_{\text{guard}}(\theta_c, \phi_c, \delta)$ to $\hat{\mathcal{W}}_s^{\text{tx}}$ in (13), the combined Tx communication and guard beams weight vectors becomes dependent on δ and η, as expressed as follows:

$$\begin{aligned} \hat{\mathcal{W}}^{\text{tx}}(\theta_c, \phi_c, \delta, \eta) = \sqrt{(1-\eta)}\, \hat{\mathcal{W}}_c^{\text{tx}}(\theta_c, \phi_c) \\ + \sqrt{\eta}\hat{\mathcal{W}}_{\text{guard}}(\theta_c, \phi_c, \delta), \end{aligned} \tag{22}$$

followed by the weight vector normalization. In order to receive an adequate backscattered signal power from the potential blocker in the intended detection area, the Rx array needs to align its beamforming towards the same direction as the Tx guard beams. Thus, the beamforming weight vector for Rx guard beams becomes:

$$\hat{\mathcal{W}}^{\text{rx}}(\theta_c, \phi_c, \delta) = \hat{\mathcal{W}}_{\text{guard}}(\theta_c, \phi_c, \delta). \tag{23}$$

B. OPTIMAL GUARD BEAMS PARAMETERS

As we consider a shared array for generating the Tx communication and sensing beams, two guard beams parameters – the guard beams separation angle δ and the power allocation coefficient η – need to be optimized to generate the sensing beams with sufficient beamforming gain while maintaining the communication performance above the specified threshold.

For communication, the primary constraint revolves around attaining the minimum required SNR at the UE to achieve a desired Modulation and Coding Scheme (MCS). The 3GPP standard [37] specifies the required spectral efficiency, which can be translated into SNR required for achieving a certain MCS index. On the other hand, the IEEE 802.11ad and IEEE 802.11ay standards utilize the required minimum received signal level and Error Vector Magnitude (EVM) parameters, respectively, in determining the MCS index [38], [39]. Since the Tx beamforming gain g_u^{tx} directly impacts the SNR χ_u, as expressed in (2) and (3), we define the minimum Tx beamforming gain of the BS to achieve a minimum required communication SNR $\chi_u^{\min}$ given a user distance d_u, expressed as:

$$g_u^{\text{tx}\min}(d_u) = \frac{\chi_u^{\min}\,(4\pi\, d_u)^2\, \sigma_u^2}{p_t\, g_u^{\text{rx}} \lambda^2}. \tag{24}$$

For the sensing requirement, the constraint is the minimum SNR required to detect a target. In an OFDM radar, the minimum SNR required to detect a target, given a probability of false alarm P_{FA}, can be expressed as [40]:

$$\chi_q^{\min} = 10^{\ln\left(1 - \sqrt[KL]{1-P_{\text{FA}}}\right)}, \tag{25}$$

where K and L denote the number of subcarriers and symbols, respectively. Using (6) and (25), the minimum combined Tx and Rx beamforming gain to achieve the required minimum

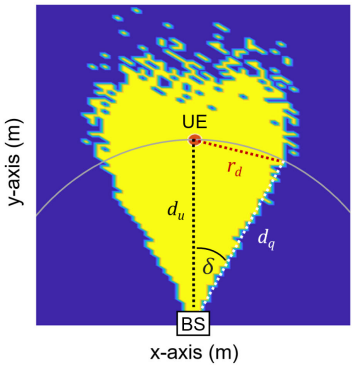

FIGURE 4. Detection range and sensing coverage.

SNR $\chi_q^{\min}$ for detecting a target with the range of d_q can be expressed as:

$$g_q^{\text{comb}^{\min}}(d_q) = \frac{\chi_q^{\min}(4\pi)^3 d_q^4 \sigma_r^2 F}{p_t \lambda^2 \rho_q}. \tag{26}$$

The detection coverage of guard beams is focused on the potential blocking area around the UE, especially the region between the BS and the UE. Therefore, the design of guard beams is tailored to scan the potential blocker on both the left and right sides of the UE. Given a communication beam direction (θ_c, ϕ_c), we define an objective function to find the optimal separation angle δ and power allocation coefficient η that maximizes the detection range r_d. Here, r_d is defined as the maximum distance from the UE to a detectable target located at the BS coverage perimeter, as illustrated in Fig. 4. Along this perimeter, the BS–target distance d_q equals the BS–UE distance d_u. The optimization problem for each set of guard beams is formulated as follows:

$$\max_{\eta,\delta} \quad r_d(d_u, \delta) \approx 2\, d_u \sin\left(\frac{\delta}{2}\right) \tag{27}$$

$$\text{s.t.} \quad g^{\text{tx}}(\theta_c, \phi_c, \delta, \eta) \geq g_u^{\text{tx}^{\min}}(d_u) \tag{27a}$$

$$g^{\text{comb}}(\theta_s, \phi_c, \delta, \eta) \geq g_q^{\text{comb}^{\min}}(d_q) \tag{27b}$$

$$\theta_s : \theta_s \in [\theta_c, \theta_c \pm \delta] \tag{27c}$$

$$\theta_c : \theta_c \in [-90^\circ + \delta, 90^\circ - \delta] \tag{27d}$$

$$\phi_c : \phi_c \in [-90^\circ + \delta, 90^\circ - \delta] \tag{27e}$$

$$\eta : \eta \in [0, 1] \tag{27f}$$

$$\delta : \delta \in [0^\circ, \delta_{\max}] \tag{27g}$$

where $g^{\text{tx}}(\theta_c, \phi_c, \delta, \eta)$ is the Tx beamforming gain in the direction of communication beam and $g^{\text{comb}}(\theta_s, \phi_c, \delta, \eta)$ represents the combined Tx–Rx beamforming gain within the coverage of guard beams, covering the azimuth $\theta_s \in [\theta_c, \theta_c \pm \delta]$. The negative or positive index indicates the left or right guard beams, respectively.

For communication, the constraint involves a Tx gain $g^{\text{tx}}(\theta_c, \phi_c, \delta, \eta)$ being at least equal to $g_u^{\text{tx}^{\min}}(d_u)$, fulfilling $\chi_u^{\min}$ for a UE at distance d_u. This constraint becomes crucial as certain η and δ combinations could result in destructive interference in the (θ_c, ϕ_c) direction. For the sensing purpose, the combined Tx and Rx gain within the guard beams coverage must be at least equal to the minimum combined Tx and Rx gain $g_q^{\text{comb}^{\min}}(d_q)$, satisfying the sensing SNR requirement $\chi_q^{\min}$ for target detection at a distance d_q.

The power allocation coefficient η ranges from 0 to 1, where higher values of η allocate more power to the guard beams, as expressed in (22). Meanwhile, δ spans from 0° to $\delta_{\max}$, representing the maximum limit for the steering angle of the guard beams. The limit of $\delta_{\max}$ is chosen considering a non-contiguous detection coverage due to applying a large δ. Furthermore, a larger δ limits the direction of the communication beam since the BS field of view is limited up to $(\theta_c, \phi_c) \in [-90^\circ + \delta, 90^\circ - \delta]$. Despite the practical field of view limitation of the UPA is ±50° [41], our evaluation extends up to ±90° limit in azimuth and elevation to provide an understanding of the behaviour of guard beams beyond the practical constraints.

IV. MULTI-STAGE DETECTION AND ESTIMATION

The sensing objective is to detect and localize dynamic potential blockers, such as people or machines in the surrounding environment, capable of shadowing the communication beams between the BS and the UE. Therefore, the system must be able to estimate the sensing parameters, i.e., range, Doppler or velocity, and DoA of a potential blocker. In a typical OFDM radar system [40], both range and Doppler information of a target are obtained simultaneously using high-resolution bins in the frequency and time (symbol) dimensions, while multiple scans in different directions are required to determine the target's DoA. However, allocating a large number of symbols for Doppler estimation is inefficient when no target is present. To enhance the efficiency of symbol utilization in detecting the potential blocker and estimating its sensing parameters, we propose a multi-stage sensing processing approach. This approach is divided into three stages: 1) Target detection, direction, and range estimation; 2) Doppler estimation; and 3) DoA estimation. Each stage requires a different number of symbols to obtain the desired accuracy.

A. SENSING SIGNAL PROCESSING

Upon receiving the backscattered signal y_s from (4), static target removal is applied to remove detection of the static clutters in the environment. It can be done using high-pass filtering or removing the Direct Current (DC) component. In this work, we consider the latter approach. The received signal after DC component removal becomes:

$$y_t(k, l) = y_s(k, l) - \frac{1}{L}\sum_{l'=1}^{L} y_s(k, l'). \tag{28}$$

In order to reduce the sampling rate, CSI accumulation is carried out across the subcarriers and symbols. This is often used in digital radars (cf. [42]) and has the impact of reducing memory consumption and complexity in the subsequent signal processing, often with a negligible impact on the

performance. The accumulation is carried out as follows:

$$\bar{y}_t(k,l) = \sum_{i=0}^{\zeta_K-1} \sum_{j=0}^{\zeta_L-1} y_r(\zeta_K k + i, \zeta_L l + j), \tag{29}$$

where ζ_K and ζ_L denote the accumulation factors across the subcarriers and symbols, respectively. The accumulation provides a coherent processing gain of $\zeta_K \zeta_L$, and a reduction in maximum unambiguous range and velocity by a factor of ζ_K and ζ_L. Since the accumulation does not impact the bandwidth or the integration time, the resolution in range and Doppler remains unaffected. The effective number of subcarriers and symbols after the accumulation becomes $K_d = K/\zeta_K$ and $L_d = L/\zeta_L$ in the respective dimensions.

We consider periodogram-based processing [40] for the computation of range-Doppler maps, derived through a one-dimensional fast Fourier transform (FFT) over symbols and inverse fast Fourier transform (IFFT) across subcarriers after static target removal. To mitigate the impact of sidelobes, a window function $\omega_{\mathrm{RD}}(k,l)$ is used. The resulting range-Doppler maps are as follows:

$$Y(a,b) = \sum_{l=0}^{L_d-1} \sum_{k=0}^{K_d-1} \omega_{\mathrm{RD}}(k,l)\bar{y}_t(k,l) e^{\frac{2\pi k}{K}a} e^{-\frac{2\pi l}{L}b}, \tag{30}$$

where a and b represent the corresponding range and Doppler bins, respectively. The estimated 2-D distance between the BS and the target q is defined as:

$$d_q = \sqrt{d_{\mathrm{rd},q}^2 - {h_{\mathrm{BS}}}^2} \tag{31}$$

where h_{BS} is the BS antenna height and $d_{\mathrm{rd},q}$ is the target distance obtained after the range-Doppler processing.

The cell averaging Constant False Alarm Rate (CFAR) detector is applied to the range-Doppler map in order to detect the targets. The CFAR determines a threshold for each Cell Under Test (CUT) based on the background noise calculated from guard cells and training cells. The threshold is expressed as follows [43]:

$$\gamma(a,b) = ({P_{\mathrm{FA}}}^{-1/N_C} - 1) p_{\mathrm{TC}}(a,b), \tag{32}$$

where $p_{\mathrm{TC}}(a,b)$ is the power in the N_C training cells. Accordingly, a target at the range-Doppler bin a and b is considered present if $|Y(a,b)|^2 > \gamma(a,b)$. The output of CFAR detection is a binary map, wherein all samples surpassing the threshold are categorized as detection ('1'), while the remaining are classified as noise ('0'). For each target detected, the centroid of the binary detection in both dimensions are calculated to estimate the target's range and velocity.

B. TARGET DETECTION, DIRECTION AND RANGE ESTIMATION

In the initial stage, the focus is on detecting a target—specifically, a potential blocker—approaching the UE. It involves estimating the coarse direction, i.e., determining whether the target is approaching from the left or right side of the UE, and conducting range estimation. The process for Stage 1 is presented in Algorithm 1. The guard beams are scanned by default in two fixed directions: left $\mathcal{D}_L$ and right $\mathcal{D}_R$, covering the area around the UE within a range of r_d. Each scan utilizes all subcarriers K to ensure accurate range estimation, based on the predefined range resolution Δr. During this stage, sensing employs a low-resolution 2D FFT-IFFT in the Doppler dimension, utilizing only a limited number of symbols, denoted as L_{S1}. This results in coarse velocity estimates. This approach is adopted to reduce the initial sensing time and signal processing load, particularly when no target is detected.

In the absence of a target, the BS continuously scans in two directions using the two sets of guard beams. It's important to note that the BS is assumed to have knowledge of the UE location, enabling it to track the UE's location and update both communication and guard beams accordingly. Upon detection of a target by one of the guard beams, the BS acquires the estimated target's range d_q based on (30) and (31), and designates its coarse direction as $\mathcal{D}_{S1} = \{\mathcal{D}_L \vee \mathcal{D}_R\}$, where $\mathcal{D}_L$ and $\mathcal{D}_R$ indicates the target detection on the left and right sides of the UE. In the case of multiple targets detected on both sides, $\mathcal{D}_{S1} = \{\mathcal{D}_L, \mathcal{D}_R\}$, subsequent Doppler and DoA estimations are performed for both sides sequentially.

Algorithm 1 Target Detection, Direction, and Range Estimation

Input: θ_c, ϕ_c, δ_{opt}, η_{opt}, K, L_{S1}
Output: d_q, $\mathcal{D}_{\mathrm{S1}}$

```
while Q = 0 do
    Scan the guard beams in D_L & D_R
    for each D do
        Tx–Rx beamforming: Ŵ^tx & Ŵ^rx                (22)(23)
        CSI collection: y_s ∈ C^(K×L_S1)               (4)
        Static clutter removal: y_t ∈ C^(K×L_S1)       (28)
        CSI accumulation: ȳ_t ∈ C^(K_d×L_dS1)          (29)
        2D FFT-IFFT: Y_S1 ∈ C^(K_d×L_dS1)              (30)
        CFAR detection: d_q                            (32)
    end
end
D_S1 ← {D_L ∨ D_R}
```

Algorithm 2 Doppler Estimation

Input: $\hat{\mathcal{W}}^{\mathrm{tx}}$, $\hat{\mathcal{W}}^{\mathrm{rx}}$, $\mathcal{D}_{S1}$, K, L_{S2}
Output: v_q

```
Scan the guard beams in D_S1 using Ŵ^tx & Ŵ^rx
CSI collection: y_s ∈ C^(K×L_S2)                       (4)
Static clutter removal: y_t ∈ C^(K×L_S2)               (28)
CSI accumulation: ȳ_t ∈ C^(K_d×L_dS2)                  (29)
2D FFT-IFFT: Y_S2 ∈ C^(K_d×L_dS2)                      (30)
CFAR detection: v_q                                    (32)
```

Algorithm 3 DoA Estimation

Input: θ_c, ϕ_c, d_q, Δp, $\mathcal{D}_{S1}$, δ, K, L_{S3}
Output: θ_q

Determine $\mathcal{R}$ (35)
Determine θ_r & ϕ_r (36),(37)
Scan the refinement beams in $\mathcal{R}$ directions
for $r \leq \mathcal{R}$ **do**
    Tx–Rx beamforming: $\hat{\mathcal{W}}^{\text{tx}}$ & $\hat{\mathcal{W}}^{\text{rx}}$ (38),(39)
    CSI collection: $y_s \in \mathbb{C}^{(K \times L_{S3})}$ (4)
    Static clutter removal: $y_t \in \mathbb{C}^{(K \times L_{S3})}$ (28)
    CSI accumulation: $\bar{y}_t \in \mathbb{C}^{(K_d \times L_{d_{S3}})}$ (29)
    2D FFT-IFFT: $Y_{S3} \in \mathbb{C}^{(K_d \times L_{d_{S3}})}$ (30)
    $|Y_r| \leftarrow |Y_{S3}|$
end
Estimate θ_q (40)

C. DOPPLER ESTIMATION

Stage 2 focuses on estimating the velocity of a target detected in the $\mathcal{D}_{S1}$ direction, as determined in Stage 1. The process for Stage 2 is outlined in Algorithm 2. In this stage, a high-resolution 2D FFT-IFFT in the Doppler dimension is employed to precisely estimate the target's radial velocity. This involves using a larger number of symbols, denoted as L_{S2} in (30), where $L_{S2} \gg L_{S1}$. The parameter L_{S2} is user-defined, which depends on the desired attainable Doppler resolution Δv. In scenarios where multiple potential blockers are detected on both sides of the guard beams, Doppler estimation is performed for each side, doubling the required symbols L_{S2}.

D. DIRECTION OF ARRIVAL ESTIMATION

The final stage aims to estimate the DoA of the potential blocker relative to the BS, denoted as θ_q. The process for Stage 3 is summarized in Algorithm 3. Given that Stage 1 provides only the coarse direction $\mathcal{D}_{S1}$ of a detected target, with the true azimuth lying within $[\theta_c : \theta_c \pm \delta]$, the maximum position error resulting from azimuth deviation obtained in Stage 1 can be expressed as:

$$\Delta p_{\mathcal{D}}(d_q) = 2\, d_q \sin\left(\frac{\delta}{2}\right). \tag{33}$$

A larger d_q and/or δ lead to a larger position estimation error. Therefore, a more refined azimuth estimation is required in Stage 3, which can be achieved by scanning multiple refinement beams within the azimuth $[0^\circ : 0^\circ \pm \delta]$. The required number of scans $\mathcal{R}$ to achieve a desired position error owing to DoA estimation error, denoted as Δp, is formulated as:

$$\mathcal{R} = \left\lceil \frac{\Delta p_{\mathcal{D}}}{\Delta p} \right\rceil. \tag{34}$$

Instead of using a fixed number of scans to obtain refined DoA estimation, we propose a dynamic $\mathcal{R}$, where the number of scans is determined based on the d_q information obtained in Stage 1. By substituting (33) to (34), the number of scans becomes a function of the target distance, as follows:

$$\mathcal{R}(d_q) = \left\lceil \frac{2d_q \sin\left(\frac{\delta}{2}\right)}{\Delta p} \right\rceil. \tag{35}$$

Therefore, with this model, a smaller d_q can reduce the number of required scans in this stage.

Each scan is performed using only a single sensing beam at a time, steered in the azimuth:

$$\theta_r = \left\{ \pm\frac{\Delta\theta_r}{2}, \pm\frac{3\Delta\theta_r}{2}, \ldots, \pm\frac{(2\mathcal{R}-1)\Delta\theta_r}{2} \right\}, \tag{36}$$

where $\Delta\theta_r = \frac{\delta}{\mathcal{R}}$ represents the angle resolution of the refinement beam. The negative or positive index is used when $\mathcal{D}_{S1} = D_{\text{L}}$ or $\mathcal{D}_{S1} = D_{\text{R}}$, respectively. The elevation ϕ_r remains constant for all $\mathcal{R}$ scans and is adjusted based on the estimated target range d_q, formulated as:

$$\phi_r(d_q) = -\tan^{-1}\left(\frac{h_{\text{BS}}}{d_q}\right) + \phi_{\text{BS}}, \tag{37}$$

where ϕ_{BS} denotes the BS antenna down-tilt angle. The beamforming weight vector of the sensing beam is defined as $\hat{\mathcal{W}}_r(\theta_r, \phi_r)$. Using (13), the weight vector of the Tx beamformer becomes:

$$\hat{\mathcal{W}}^{\text{tx}} = \sqrt{(1-\eta)}\, \hat{\mathcal{W}}_c(\theta_c, \phi_c) + \sqrt{\eta}\, \hat{\mathcal{W}}_r(\theta_r, \phi_r), \tag{38}$$

followed by the weight vector normalization. The Rx beamformer is set to receive in the direction of the sensing beam with the beamforming vector of:

$$\hat{\mathcal{W}}^{\text{rx}} = \hat{\mathcal{W}}_r(\theta_r, \phi_r). \tag{39}$$

The DoA estimation is carried out using low-resolution 2D FFT-IFFT in the Doppler dimension, where only a few OFDM symbols are used. For each scan, L_{S3} symbols are used in (30), where $L_{S3} \ll L_{S2}$. The investigation into the minimum number of symbols L_{S3} that still yields accurate DoA estimation is detailed in Section V-D. Using (4) and (30), the collected CSI becomes $y_s \in \mathbb{C}^{(K \times L_{S3})}$, and the resulting periodogram becomes $Y_{S3} \in \mathbb{C}^{(K_d \times L_{d_{S3}})}$, respectively. The BS computes the periodogram magnitude $|Y_r| = |Y_{S3}|$ of all $\mathcal{R}$ scans, and estimates the azimuth of potential blocker θ_q by choosing the θ_r resulting in the maximum $|Y_r|$, as expressed below:

$$\theta_q = \arg\max\{|Y_1|, \ldots, |Y_{\mathcal{R}}|\}. \tag{40}$$

Notably, practical constraints such as array/hardware imperfections and beamforming quantization influence the beam pattern and its angular resolution [27].

The BS localizes the potential blocker in the x–y axis by using d_q obtained in Stage 1 and θ_q obtained in Stage 3, as follows:

$$p_{x,y} = \left(d_q \sin\left(\theta_q\right), d_q \cos\left(\theta_q\right)\right). \tag{41}$$

Meanwhile, v_q is obtained through Stage 2. Using this information, the BS can promptly and proactively identify

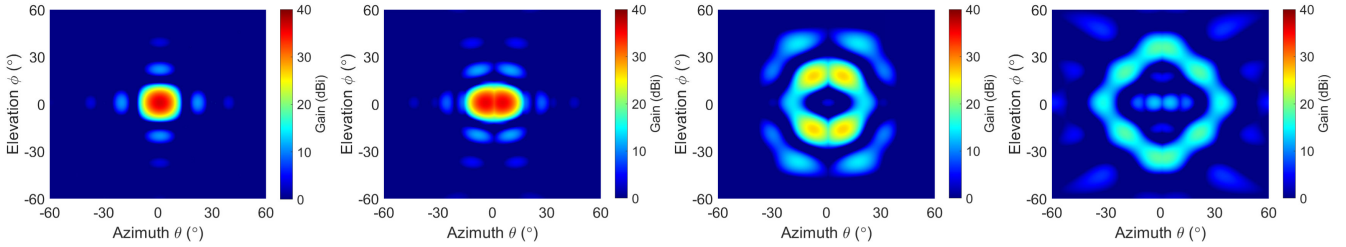

(a) $\delta = 0°$ or $\eta = 0$ (no guard beams) (b) $\delta = 10°$ (c) $\delta = 20°$ (d) $\delta = 30°$

FIGURE 5. Combined Tx–Rx gain of guard beams over various δ with $(\theta_c, \phi_c) = (0°, 0°)$, $N_G = 5$ and $\eta = 0.7$.

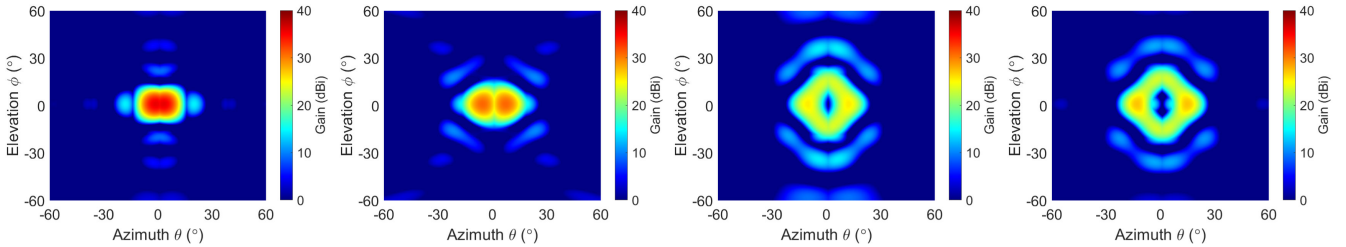

(a) $\eta = 0.25$ (b) $\eta = 0.5$ (c) $\eta = 0.75$ (d) $\eta = 1$

FIGURE 6. Combined Tx–Rx gain of guard beams over various η with $(\theta_c, \phi_c) = (0°, 0°)$, $N_G = 5$ and $\delta = 15°$.

potential link blockages upon entering the coverage area. This enables immediate follow-up actions to mitigate the blockage, such as initiating a handover as suggested in [25] and [44]. However, these mitigation strategies are outside the scope of this paper.

V. NUMERICAL RESULTS AND ANALYSIS

A. SIMULATION PARAMETERS

We carried out simulations to evaluate the sensing performance of guard beams, including the detection coverage area and estimation accuracy, and the impact of guard beams on the communication performance. Detailed simulation parameters are provided in Table 1. We consider an ISAC BS placed at a height of 15 m. Both Tx and Rx arrays of the BS employ $\text{UPA}_{(8\times8)}$, tilted down 10° to cover UEs at a lower height. Static UE and mobile blockers, at a height of 1.5 m, are placed within the field of view of the BS.

The BS transmits the OFDM waveform operating at $f_c = 26$ GHz with the bandwidth B of 384 MHz and $K = 1600$ subcarriers, with the subcarrier spacing Δf being 240 kHz. The OFDM symbol duration T_p is 4.46 μs including the cyclic prefix duration. The transmit power p_t is kept fixed at 20 dBm with the beamforming gain depending on the Tx weight vector. Meanwhile, the UE uses $\text{UPA}_{(2\times2)}$ to beamform towards the BS and has the noise figure F_u of 7 dB.

The potential blocker detection is performed within a coherent processing interval spanning L symbols, with varying numbers of symbols used in different sensing stages, as discussed in Section IV. Taking the maximum number of symbols used in each stage mentioned in Table 1, the detection and sensing estimation can be performed within 11 ms, which is relatively faster than the potential blocker's movement. The probability of false alarm P_{FA} is set to be 10^{-6}, with 10 training cells and 4 guard cells in both range and Doppler dimensions used for CFAR detection. The radar noise figure F_r is 7 dB. For our analysis, we assume a single point reflection from each potential blocker, characterized by a fixed RCS value of $\rho_q = 1$ for human targets [43].

TABLE 1. Simulation parameters.

Parameter	Value
BS height (h_{BS})	15 m
BS antenna tilting angle (ϕ_{BS})	10°
BS transmit power (p_T)	20 dBm
BS array size ($M \times N$)	8×8
No. of sub-guard-beams (N_G)	5
Frequency carrier (f_c)	26.0 GHz
Bandwidth (B)	384 MHz
Number of subcarriers (K)	1600
Number of OFDM symbols: (L)	
Stage 1 (L_{S1})	40 – 640
Stage 2 (L_{S2})	1600
Stage 3 (L_{S3})	40 – 240
Downsampling factor (ζ_K & ζ_L)	8
Subcarrier spacing (Δf)	240 kHz
Symbol period (T_p)	4.46 μs
Probability of false alarm (P_{FA})	10^{-6}
Radar noise figure (F_r)	7 dB
Potential blocker's RCS (ρ_q)	1
Potential blocker's velocity	1 – 3 m/s
UE height (h_{BS})	1.5 m
UE array size ($M \times N$)	2×2
UE noise figure (F_u)	7 dB

B. GUARD BEAMS PARAMETERS EVALUATION

In this section, we assess two key parameters influencing the generation guard beams: the separation angle δ and the power allocation coefficients η. These parameters directly impact the beam shape, consequently influencing the attainable

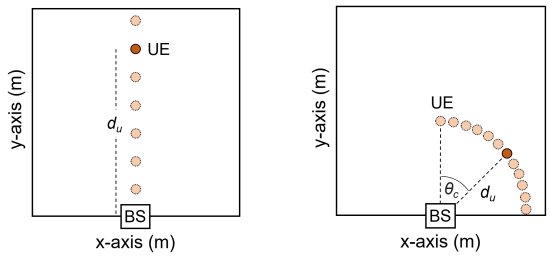

(a) Evaluated UE positions along d_u

(b) Evaluated UE positions along θ_c

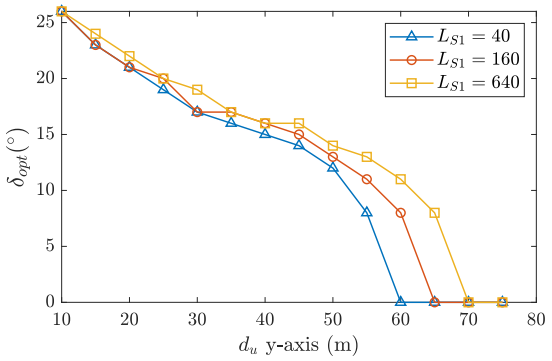

(c) Optimal guard beams steering angle over the BS–UE distance d_u in y-axis (θ_c = 0°)

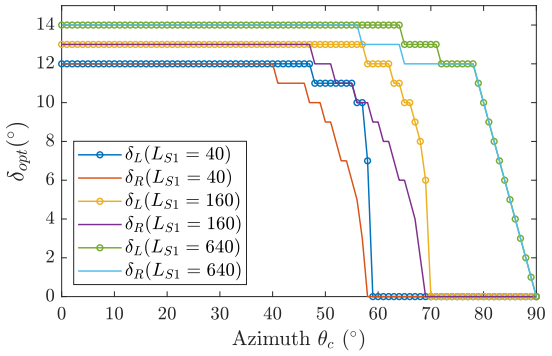

(d) Optimal guard beams steering angle over different UE azimuth θ_c (d_u = 50 m & ϕ_c = 0°)

FIGURE 7. δ_{opt} **evaluation for different UE positions.**

gain in both communication and sensing directions. For the evaluation, we consider $N_G = 5$ sub-beams on each side of the guard beams. Fig. 5 and Fig. 6 depict the combined Tx–Rx beam patterns of communication and guard beams for different δ and η values, respectively. The communication beam is steered at $(\theta_c, \phi_c) = (0°, 0°)$ with the combined left and right guard beams surrounding (θ_c, ϕ_c).

Without guard beams, a strong Tx–Rx beamforming gain is observed in (θ_c, ϕ_c) direction, as depicted in Fig. 5(a). Applying guard beams with $\delta = 10°$ extends the sensing coverage in the azimuth directions, as illustrated in Fig. 5(b). As the guard beams are steered away from the communication beam, a noticeable coverage gap emerges between the communication beam and each sub-guard beam. Moreover, the communication gain undergoes a significant reduction with increasing δ, as observed in Fig. 5(c) and Fig. 5(d). Increasing η also influences the beam patterns, as presented in Fig. 6. A larger η yields increased gain in the sensing directions while concurrently reducing the communication gain. These findings highlight the crucial need to identify optimal values for δ and η that satisfy both communication and sensing constraints.

To obtain the optimal parameters of guard beams, we consider the minimum required communication SNR $\chi_u^{\min}$, obtaining the highest MCS index for 64-QAM based on 3GPP TS 38.214 [37], and the minimum required sensing SNR $\chi_q^{\min}$ with $L_{S1} = 40$, 160 and 640 symbols. Using the greedy optimization algorithm to solve the problem in (27), we evaluate the optimal steering angle δ_{opt} for different UE positions, as presented in Fig. 7. In Fig. 7(a), the δ_{opt} over d_u in y-axis, where $\theta_c = 0°$, is assessed. The results are presented in Fig. 7(c). Note that the left and the right guard beams are symmetrical as $\theta_c = 0°$, thereby δ_{opt} is applicable to both sides.

At shorter distances, a large δ_{opt} can be applied, since both the communication SNR $\chi_u^{\min}$ at θ_c and sensing SNR $\chi_q^{\min}$ along $[\theta_c : \theta_c \pm \delta]$ constraints are satisfied at a short d_u. As the d_u increases, the BS requires more beamforming gain in the user direction to meet the $\chi_u^{\min}$ given a fixed transmit power p_t. Consequently, the δ_{opt} becomes smaller to concentrate the beamforming around the θ_c direction. The same descending trend is observed in each L_{S1}, where using more symbols enables the guard beams to have a larger δ_{opt}, thanks to a more relaxed $\chi_q^{\min}$ constraint. Beyond a certain d_u, the δ_{opt} for each L_{S1} reaches 0° as the constraints are no longer fulfilled, indicating the distance limit of the guard beams.

Besides the impact of d_u, we also evaluate the influence of communication beam azimuth θ_c on δ_{opt}, as depicted in Fig. 7(b). By maintaining a constant $d_u = 50$ m and ϕ_c, we evaluate the δ_{opt} for both the left and right guard beams over different θ_c, as presented in Fig. 7(d). The results show that both the left and the right guard beams maintain the same δ_{opt} until a certain θ_c. Beyond that point, the δ_{opt} gradually decreases as θ_c increases. This declining trend in all evaluated number of symbols L_{S1} results from the fact that the increasing θ_c corresponds to a decrease in $g^{\text{tx}}(\theta_c, \phi_c)$. Consequently, δ_{opt} is reduced to concentrate the beamforming gain around the communication beam, fulfilling the communication constraint. It is important to note that the trends in Fig. 7(d) are symmetrical for the negative θ_c.

C. DETECTION RANGE AND SENSING COVERAGE AREA

We assess the sensing coverage area, indicating the region inside the BS perimeter where potential blockers are detectable for a given a UE position. Additionally, we also evaluate the detection range, which indicates the maximum distance between the UE and a detectable target located at the perimeter. Detection is performed for each target position in the x–y grid area with a 0.5 m distance between points. The sensing coverage area highly depends on the UE location, as the steering angles of the guard beams follow the communication beam direction.

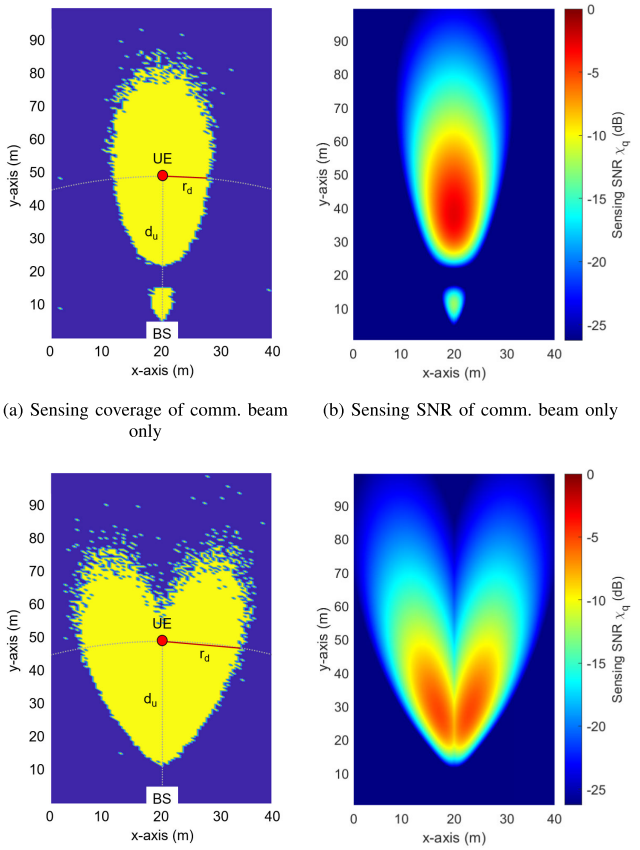

(a) Sensing coverage of comm. beam only

(b) Sensing SNR of comm. beam only

(c) Sensing coverage with guard beams

(d) Sensing SNR with guard beams

FIGURE 8. Sensing coverage and sensing SNR comparison.

Fig. 8 illustrates the comparison between sensing coverage area and sensing SNR χ_q for detection using both communication-beam-only, as the baseline, versus those incorporating guard beams. The example is evaluated for the UE at a distance $d_u = 50$ m from the BS with $\theta_c = 0°$, using $L_{S1} = 160$ coherent symbols. The yellow areas in Fig. 8(a) and Fig. 8(c) indicate the regions where the target is detectable. The results demonstrate that using guard beams enhances both the detection range r_d and the sensing coverage in the potential blocking area, compared to the detection using solely the communication beam. In both cases, the detection coverage corresponds to the sensing SNR heatmap, as presented in Fig. 8(b) and 8(d). In the communication-beam-only case, the beam is concentrated toward the UE direction. On the other hand, the presence of guard beams directs beams to cover the left and right sides of the UE, extending its sensing coverage.

Fig. 9 and Fig. 10 show the comparison of achievable target detection range r_d and sensing coverage area between the communication-beam-only and the one using guard beams. These metrics are evaluated across various BS–UE distances d_u on the y-axis with $\theta_c = 0°$. The results indicate that the detection range and the sensing coverage area increase as the UE moves away from the BS, owing to a larger

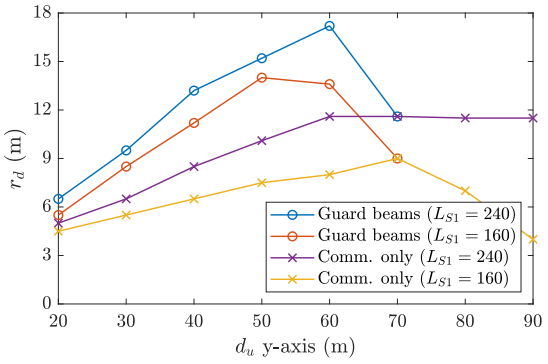

FIGURE 9. Max. detection range over BS–UE distance d_u ($\theta_c = 0°$).

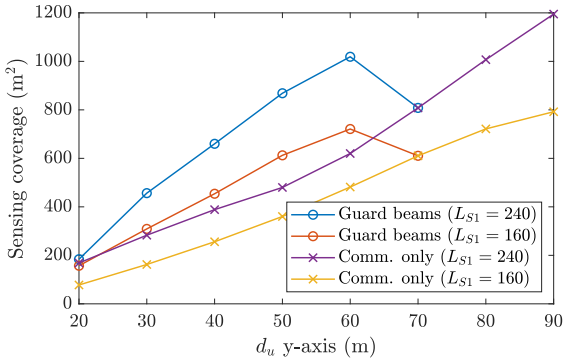

FIGURE 10. Sensing coverage area over BS–UE distance d_u ($\theta_c = 0°$).

projected beam. Employing more coherent symbols improved the sensing coverage, as observed in both cases.

The results demonstrate that using guard beams provides significant advantages compared to relying solely on the communication beam, offering over 1.5 times greater average detection range and sensing coverage area. Beyond d_u of 60 m, the detection range and sensing coverage area of guard beams converge with the baseline method, as observed in both $L_{S1} = 160$ and $L_{S1} = 240$ cases. In these distances, the guard beams can no longer be applied due to the inability to fulfil the communication and sensing constraints given the fixed BS transmit power, as discussed earlier in Section V-B. Consequently, sensing relies only on the communication beam beyond this point.

D. RANGE, VELOCITY AND DOA ESTIMATION ACCURACY

The use of guard beams only influences the channel gain in the desired sensing area without compromising the accuracy of range and velocity estimation. The only parameters affecting the range and velocity estimation accuracy are the number of subcarriers K and symbols L_{S2} used in Stage 2, respectively. Table 2 presents the range and velocity estimation error of all compared scanning methods, with the communication-beam-only and exhaustive scanning methods serving as baselines. The results align with the expected range and velocity resolutions of 78.07 cm and 80.82 cm/s, obtained using $K = 1600$ subcarriers and $L_{S2} = 1600$ symbols. The estimation accuracy holds relevance only when the target

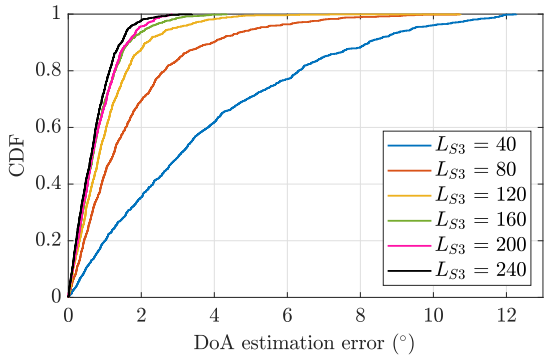

FIGURE 11. DoA estimation error of dynamic $\mathcal{R}$ approach.

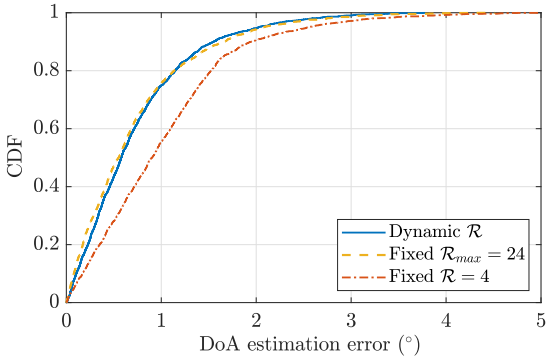

FIGURE 12. DoA estimation error comparison of different refinement methods ($L_{S3} = 160$ symbols).

falls within the coverage area of each scanning method. Having this range resolution allows differentiation between two persons, and the velocity resolution is sufficient for discerning the typical average human walking speed of 1.43 m/s [45].

We evaluate the DoA estimation error, defined as the discrepancy between the estimated potential blocker's azimuth (40) obtained in Stage 3 and the actual value. We place the UE at $d_u = 50$ m with $\theta_c = 0°$ from the BS and randomly distribute a blocker within the potential blocking area. We apply our dynamic $\mathcal{R}$ scanning approach and evaluate the estimation error for various numbers of symbols L_{S3}. Fig. 11 shows the Cumulative Distribution Function (CDF) of DoA estimation error for L_{S3} ranging from 40 to 240 symbols. It shows that using more integrated symbols reduces the angle estimation error, attributed to a lower sensing SNR $\chi_q^{\min}$ requirement (25). The DoA estimation error starts converging at $L_{S3} = 160$ symbols, as using beyond that number provides comparable DoA estimation errors.

We compare the DoA estimation error of our proposed dynamic scanning $\mathcal{R}(d_q)$ approach and the fixed scanning approach using a maximum number of scans $\mathcal{R}_{\max}$. For both approaches, the number of scans $\mathcal{R}$ is set to achieve a desired position accuracy of $\Delta p = \pm 0.5$ m. Fig. 12 depicts the CDF of angle estimation errors comparison among two approaches, where the maximum number of scans for the UE positioned at $d_u = 50$ m and $\theta_c = 0°$ is $\mathcal{R}_{\max} = 24$, making it the lower bound of the DoA estimation error. It is shown that using only $\mathcal{R} = 4$ scans leads to a larger DoA estimation error as the angle resolution between the tested beams decreases. Meanwhile, our proposed approach can achieve the same performance as the lower bound requiring $\mathcal{R}_{\max} = 24$ by using only $\mathcal{R} = 15$ scans on average.

TABLE 2. Range and velocity estimation.

Sensing method	Range est. error	Velocity est. error
Exhaustive scan	78.01 cm	80.57 cm/s
Guard beams	78.19 cm	80.33 cm/s
Comm. beam only	78.11 cm	80.42 cm/s

TABLE 3. Computational complexity of sensing signal processing.

Sensing method	Complexity of range-Doppler est.
Exhaustive scan	$\mathcal{O}\big(N_{\text{exh}} L_{d_{S2}} \log(N_{\text{exh}} L_{d_{S2}})\big)$
Guard beams (1 side detection)	$\mathcal{O}\big((2L_{d_{S1}} + L_{d_{S2}}) \log(2L_{d_{S1}} + L_{d_{S2}})\big)$
Guard beams (2 sides detection)	$\mathcal{O}\big(2(L_{d_{S1}} + L_{d_{S2}}) \log(2(L_{d_{S1}} + L_{d_{S2}}))\big)$
Comm. beam only	$\mathcal{O}\big(L_{d_{S2}} \log(L_{d_{S2}})\big)$

E. COMPLEXITY OF SENSING SIGNAL PROCESSING

We evaluate the complexity of sensing signal processing of each scanning method based on the number required subcarriers and symbols for range-Doppler estimation. However, only the number of required symbols are considered for the comparison since all sensing methods use the same number of subcarriers. By taking $\mathcal{O}\big(N \log(N)\big)$ as the complexity of an FFT process over N samples [46], Table 3 presents the complexity of range-Doppler estimation as function of required symbols after CSI accumulation, $L_{d_{S1}} = L_{S1}/\zeta_L$ and $L_{d_{S2}} = L_{S2}/\zeta_L$, of each scanning method.

The exhaustive approach requires N_{exh} times L_{S2} symbols for simultaneous detection range-Doppler estimation of a potential blocker throughout the entire area. In contrast, by applying multi-stage sensing pipeline, the guard beams approach by default requires only two times L_{S1} symbols to scan in both left and right directions. Larger symbols L_{S2} are required only when a potential blocker is detected, ensuring accurate Doppler estimation. Taking $N_{\text{exh}} = 16$ scans, $L_{S1} = 160$ symbols, and $L_{S2} = 1600$ symbols, in the case of multiple blockers detected on both sides, the guard beams only requires 13.83% of the symbols needed by the exhaustive scan. This highlights the efficiency of multi-stage sensing implementation on the guard beams, particularly in reducing the required symbols, accelerating the estimation process, and subsequently minimizing sensing signal processing. The communication-beam-only approach requires the least number of symbols for range-Doppler estimation. However, it lacks the capability to estimate the DoA.

F. IMPACT OF GUARD BEAM ILLUMINATION ON COMMUNICATION CHANNEL

The presence of a potential blocker near the LoS link between BS–UE influences the multipath propagation, causing interference at the UE. We define the interference zone as the area

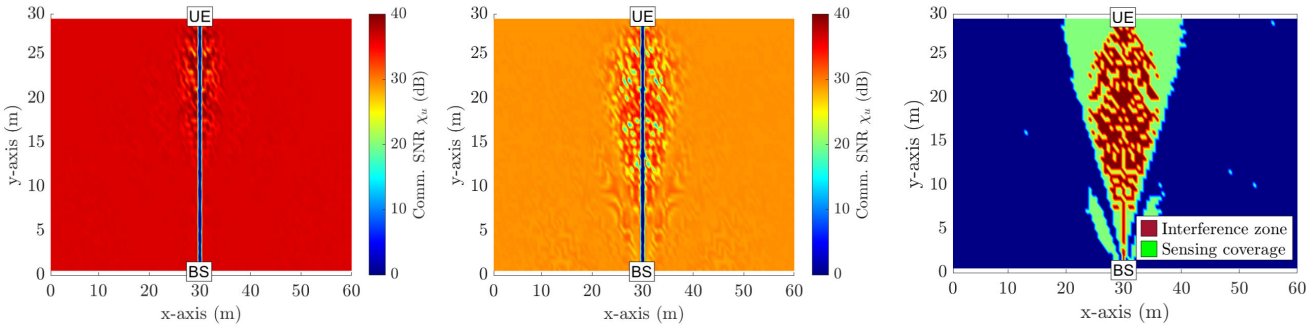

(a) Comm. SNR fluctuation of the comm. only

(b) Comm. SNR fluctuation with guard beams

(c) Interference zone and sensing coverage area with guard beams

FIGURE 13. **The interference zone where the communication SNR is influenced by the presence of an object or person in the vicinity of LoS path ($d_u = 30$ m, $\theta_c = 0°$).**

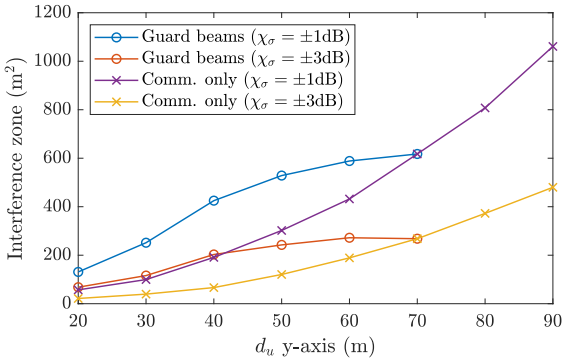

FIGURE 14. **Interference zone over BS–UE distance ($\theta_c = 0°$).**

where the SNR is influenced by the presence of an object or person. The communication performance is evaluated through the downlink communication SNR χ_u, defined in (3). Fig. 13 compares the communication SNR performance resulting from the presence of a target around the LoS link for scenarios without and with the guard beams. The color in each point represents the SNR value, accounting for a dominant LoS path and a NLoS path resulting from the single-point target scattering at the specified position.

Fig. 13(a) and Fig. 13(b) describe the fluctuation of communication SNR due to the presence of potential blocker in the evaluated area, comparing scenarios without and with guard beams, respectively. The regions with stable SNR indicate the non-interference zone, observed when the target is distant from the LoS link. In these regions, the NLoS component is relatively weaker than the LoS one, resulting in a dominant LoS channel. When the target is close to the LoS path, the NLoS component resulting from the target's reflection becomes stronger, leading to constructive and destructive interference at the UE. When using communication-beam-only, the interference zone is observed near the UE position, as illustrated in Fig. 13(a). Employing the guard beams extends the interference zones due to a larger illumination area, as shown in Fig. 13(b).

Fig. 14 presents the size of interference zone, evaluated over BS–UE distance with $\theta_c = 0°$. We apply the SNR fluctuation threshold χ_σ, indicating the SNR fluctuation tolerability due to the interference from the target. The interference area is calculated when the SNR is beyond $\bar{\chi}_0 \pm \chi_\sigma$, where $\bar{\chi}_0$ denotes the average SNR for the LoS path. At the same d_u, the guard beams results in a larger interference zone compared to the communication only. Both the lower beamforming gain in the LoS direction and the wider illumination around the LoS direction contribute to a larger interference zone. A higher tolerable SNR fluctuation threshold χ_σ reduces the size of interference zone for both cases without and with the guard beams. Nevertheless, the impacted interference zone still lies within the sensing coverage area of guard beams, as shown in Fig. 13(c). In this figure, the interference zone indicates the area where the UE experiences the SNR fluctuation of up to 3 dB, while the sensing coverage area indicates the detectability of the target when using $L_{S1} = 160$ symbols. It shows the efficacy of guard beams in protecting the communication link from being impacted by the presence of potential blocker, particularly near the LoS path.

G. COMPROMISE ON COMMUNICATION PERFORMANCE

Besides the fact that wider illumination of guard beams causes the communication SNR fluctuation, we also analyze the impact of sharing the array resources to generate communication and guard beams on the achievable SNR χ_u. As depicted in Fig. 13(a) and Fig. 13(b), using only the communication beam yields a higher SNR than that with the guard beams, thanks to a larger beamforming gain towards the UE. Fig. 15 compares the communication SNR performance between scenarios using communication beam only and those incorporating guard beams at different distances d_u. In the first case, the changes in the BS–UE distance significantly influence the SNR. On the contrary, the latter preserves similar SNR performance for different BS–UE distances, guaranteeing the value that suffices the communication SNR requirement while optimizing the array resource to enhance the sensing coverage.

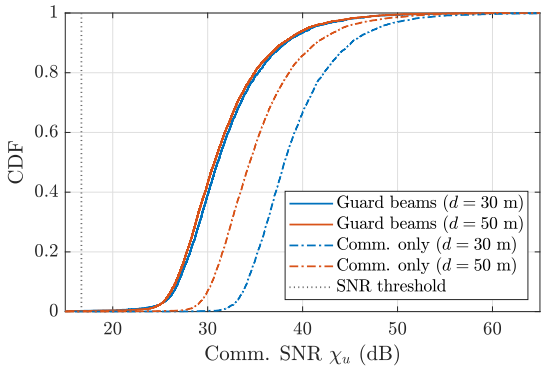

FIGURE 15. Communication SNR for various d_u ($\theta_c = 0°$).

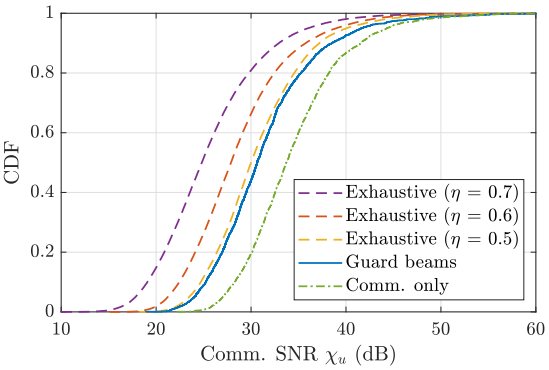

FIGURE 16. Communication SNR performance of various sensing methods.

We also evaluate the communication performance of the exhaustive scan approach as the baseline for the grid-search method. While the communication-beam-only and the guard beams approaches are designed to detect targets around the UE, the exhaustive scan aims to scan the entire environment within the BS field of view. For the exhaustive scan approach, we consider $N_{\text{exh}} = 64$ scans into 8×8 grid area in both azimuth and elevation directions, based on a pre-defined codebook. The communication beam is steered towards the UE, while each sensing beam is sequentially steered based on the codebook. The Tx beamformer applies (13) to generate both the Tx communication and sensing beams, while the Rx beamformer uses (14) to generate the Rx sensing beam. The η is set to a minimum of 0.5 to distribute power equally among the communication and sensing beams. The UE is randomly positioned in a range of 20–60 m within the BS field of view. The same fixed transmit power is applied across all methods for fair comparison.

Fig. 16 shows the CDF of communication SNR, comparing the three sensing approaches. The SNR performance of the communication-beam-only method serves as the upper bound since the Tx beam is only focused on the UE direction, gaining the maximum achievable beamforming in this direction. At the 50$^{\text{th}}$ percentile, the communication SNR when applying the guard beams experiences a reduction of $\sim$3 dB compared to the communication-only case, while the exhaustive approach with a balanced sensing and communication power ($\eta = 0.5$) exhibits a 3.7 dB lower SNR than the communication-only case. Nevertheless, a larger η might be necessary to further improve sensing channel gain for detecting the distant target when using the exhaustive approach, resulting in further communication SNR reduction. Applying $\eta = 0.6$ and $\eta = 0.7$ results in SNR degradations of 5.8 dB and 8.9 dB, respectively, compared to the communication-only case, as the beamforming gain in the direction of the UE decreases with increasing η. This highlights the importance of optimizing guard beams to minimize the reduction in communication SNR within a shared array used for both communication and sensing.

VI. CONCLUSION

We present a UE-centered ISAC approach that enables simultaneous communication with the UE while sensing the area around it. Leveraging guard beams enhances sensing coverage in the UE's vicinity, facilitating the detection of potential blockers without the need for exhaustive scanning of the entire environment. We propose guidelines for generating guard beams and optimizing the beamforming parameters to maximize sensing coverage while meeting communication performance constraints. Implementing multi-stage detection and parameter estimation on guard beams significantly reduces the computational complexity of signal processing compared to exhaustive grid searching, while maintaining comparable sensing accuracy. The optimized guard beams maintains SNR performance, demonstrating their effectiveness in balancing array resource allocation within a shared analog array system to generate multiple beams for communication and sensing purposes.

The UE-centered ISAC approach is ideal for scenarios where full environmental sensing is not required. Apart from the blockage detection, this approach can improve both user and environmental safety by enabling proximity detection for communication users, as envisioned in [9] and [10]. For instance, employing guard beams to assist communication with autonomous robots and guided vehicles in a factory setting can extend the safety perimeter against approaching objects or humans. In ground-to-air Unmanned Aerial Vehicle (UAV) communication, guard beams can expand the UAV's safe zone against nearby flying objects, without the need to scan the entire airspace. Adjusting guard beams and sensing parameters, such as sub-beam power, and tailoring optimization problems for diverse use cases are necessary and represent potential areas for future development.

REFERENCES

[1] T. S. Rappaport, S. Sun, R. Mayzus, H. Zhao, Y. Azar, K. Wang, G. N. Wong, J. K. Schulz, M. Samimi, and F. Gutierrez, "Millimeter wave mobile communications for 5G cellular: It will work!" *IEEE Access*, vol. 1, pp. 335–349, 2013.

[2] C. Slezak, V. Semkin, S. Andreev, Y. Koucheryavy, and S. Rangan, "Empirical effects of dynamic human-body blockage in 60 GHz communications," *IEEE Commun. Mag.*, vol. 56, no. 12, pp. 60–66, Dec. 2018.

[3] K. C. Joshi, R. Hersyandika, and R. V. Prasad, "Association, blockage, and handoffs in IEEE 802.11ad-based 60-GHz picocells—A closer look," *IEEE Syst. J.*, vol. 14, no. 2, pp. 2144–2153, Jun. 2020.

[4] H. Alidoustaghdam, A. Kokkeler, and Y. Miao, "Contact-free human posture estimation: An analysis of the influence of mmWave array polarization," in *Proc. 34th Gen. Assem. Scientific Symp. Int. Union Radio Sci. (URSI GASS)*, Aug. 2021, pp. 1–4.

[5] X. Zhao, Q. Wang, S. Li, S. Geng, M. Wang, S. Sun, and Z. Wen, "Attenuation by human bodies at 26- and 39.5-GHz millimeter wavebands," *IEEE Antennas Wireless Propag. Lett.*, vol. 16, pp. 1229–1232, 2017.

[6] F. Dong, F. Liu, Y. Cui, W. Wang, K. Han, and Z. Wang, "Sensing as a service in 6G perceptive networks: A unified framework for ISAC resource allocation," *IEEE Trans. Wireless Commun.*, vol. 22, no. 5, pp. 3522–3536, May 2023.

[7] X. Fang, W. Feng, Y. Chen, N. Ge, and Y. Zhang, "Joint communication and sensing toward 6G: Models and potential of using MIMO," *IEEE Internet Things J.*, vol. 10, no. 5, pp. 4093–4116, Mar. 2023.

[8] Y. Cui, F. Liu, X. Jing, and J. Mu, "Integrating sensing and communications for ubiquitous IoT: Applications, trends, and challenges," *IEEE Netw.*, vol. 35, no. 5, pp. 158–167, Sep. 2021.

[9] J. A. Zhang, M. L. Rahman, K. Wu, X. Huang, Y. J. Guo, S. Chen, and J. Yuan, "Enabling joint communication and radar sensing in mobile networks—A survey," *IEEE Commun. Surveys Tuts.*, vol. 24, no. 1, pp. 306–345, 1st Quart., 2022.

[10] S. Mandelli, M. Henninger, M. Bauhofer, and T. Wild, "Survey on integrated sensing and communication performance modeling and use cases feasibility," in *Proc. 2nd Int. Conf. 6G Netw. (6GNet)*, Oct. 2023, pp. 1–8.

[11] X. Liu, X. Li, K. Zheng, and J. Liu, "AoI minimization of ambient backscatter-assisted EH-CRN with cooperative spectrum sensing," *Comput. Netw.*, vol. 245, May 2024, Art. no. 110389.

[12] Y. Liu, T. Wang, Y. Jiang, and B. Chen, "Harvesting ambient RF for presence detection through deep learning," *IEEE Trans. Neural Netw. Learn. Syst.*, vol. 33, no. 4, pp. 1571–1583, Apr. 2022.

[13] J. A. Zhang, A. Cantoni, X. Huang, Y. J. Guo, and R. W. Heath, "Joint communications and sensing using two steerable analog antenna arrays," in *Proc. IEEE 85th Veh. Technol. Conf. (VTC Spring)*, Jun. 2017, pp. 1–5.

[14] J. A. Zhang, X. Huang, Y. J. Guo, J. Yuan, and R. W. Heath, "Multibeam for joint communication and radar sensing using steerable analog antenna arrays," *IEEE Trans. Veh. Technol.*, vol. 68, no. 1, pp. 671–685, Jan. 2019.

[15] H. Alidoustaghdam, A. Kokkeler, and Y. Miao, "Sparse tiled planar array: The shared multibeam aperture for millimeter-wave joint communication and sensing," *Electronics*, vol. 12, no. 14, p. 3115, Jul. 2023.

[16] W. Zhou, R. Zhang, G. Chen, and W. Wu, "Integrated sensing and communication waveform design: A survey," *IEEE Open J. Commun. Soc.*, vol. 3, pp. 1930–1949, 2022.

[17] Y. Oguma, T. Nishio, K. Yamamoto, and M. Morikura, "Performance modeling of camera-assisted proactive base station selection for human blockage problem in mmWave communications," in *Proc. IEEE Wireless Commun. Netw. Conf.*, Apr. 2016, pp. 1–7.

[18] Y. Koda, K. Nakashima, K. Yamamoto, T. Nishio, and M. Morikura, "Handover management for mmWave networks with proactive performance prediction using camera images and deep reinforcement learning," *IEEE Trans. Cognit. Commun. Netw.*, vol. 6, no. 2, pp. 802–816, Jun. 2020.

[19] D. Korpi, P. Yli-Opas, M. R. Jaramillo, and M. A. Uusitalo, "Visual detection-based blockage prediction for beyond 5G wireless systems," in *Proc. 2nd 6G Wireless Summit (6G SUMMIT)*, Mar. 2020, pp. 1–5.

[20] G. Charan, M. Alrabeiah, and A. Alkhateeb, "Vision-aided 6G wireless communications: Blockage prediction and proactive handoff," *IEEE Trans. Veh. Technol.*, vol. 70, no. 10, pp. 10193–10208, Oct. 2021.

[21] U. Demirhan and A. Alkhateeb, "Radar aided proactive blockage prediction in real-world millimeter wave systems," in *Proc. IEEE Int. Conf. Commun.*, May 2022, pp. 4547–4552.

[22] D. Marasinghe, N. Rajatheva, and M. Latva-Aho, "LiDAR aided human blockage prediction for 6G," in *Proc. IEEE Globecom Workshops (GC Wkshps)*, Dec. 2021, pp. 1–6.

[23] M. Alrabeiah and A. Alkhateeb, "Deep learning for mmWave beam and blockage prediction using sub-6 GHz channels," *IEEE Trans. Commun.*, vol. 68, no. 9, pp. 5504–5518, Sep. 2020.

[24] Z. Ali, A. Duel-Hallen, and H. Hallen, "Early warning of mmWave signal blockage and AoA transition using sub-6 GHz observations," *IEEE Commun. Lett.*, vol. 24, no. 1, pp. 207–211, Jan. 2020.

[25] S. Wu, M. Alrabeiah, C. Chakrabarti, and A. Alkhateeb, "Blockage prediction using wireless signatures: Deep learning enables real-world demonstration," *IEEE Open J. Commun. Soc.*, vol. 3, pp. 776–796, 2022.

[26] R. Hersyandika, Y. Miao, and S. Pollin, "Guard beam: Protecting mmWave communication through in-band early blockage prediction," in *Proc. IEEE Global Commun. Conf.*, Dec. 2022, pp. 4093–4098.

[27] Y. Luo, J. A. Zhang, X. Huang, W. Ni, and J. Pan, "Optimization and quantization of multibeam beamforming vector for joint communication and radio sensing," *IEEE Trans. Commun.*, vol. 67, no. 9, pp. 6468–6482, Sep. 2019.

[28] Y. Luo, J. A. Zhang, X. Huang, W. Ni, and J. Pan, "Multibeam optimization for joint communication and radio sensing using analog antenna arrays," *IEEE Trans. Veh. Technol.*, vol. 69, no. 10, pp. 11000–11013, Oct. 2020.

[29] C. B. Barneto, T. Riihonen, S. D. Liyanaarachchi, M. Heino, N. González-Prelcic, and M. Valkama, "Beamformer design and optimization for joint communication and full-duplex sensing at mm-waves," *IEEE Trans. Commun.*, vol. 70, no. 12, pp. 8298–8312, Dec. 2022.

[30] Y. Zhuo, Z. Sha, and Z. Wang, "Multibeam joint communication and radar sensing: Beamforming design and interference cancellation," *IEEE Commun. Lett.*, vol. 26, no. 8, pp. 1888–1892, Aug. 2022.

[31] *Service Requirements for the 5G System (Release 19)*, document TS 22.261, Version 19.7.0, 3GPP, 2024.

[32] *Study on New Radio Access Technology Physical Layer Aspects (Release 14)*, document TR 38.802, Version 14.2.0, 3GPP, 2017.

[33] S. A. Hassani, V. Lampu, K. Parashar, L. Anttila, A. Bourdoux, B. V. Liempd, M. Valkama, F. Horlin, and S. Pollin, "In-band full-duplex radar-communication system," *IEEE Syst. J.*, vol. 15, no. 1, pp. 1086–1097, Mar. 2021.

[34] *5G-NR Base Station (BS) Radio Transmission and Reception (Release 18)*, document TS 38.104, 2024, Version 18.6.0, 3GPP, 2024.

[35] W. Tan, S. D. Assimonis, M. Matthaiou, Y. Han, X. Li, and S. Jin, "Analysis of different planar antenna arrays for mmWave massive MIMO systems," in *Proc. IEEE 85th Veh. Technol. Conf. (VTC Spring)*, Jun. 2017, pp. 1–5.

[36] R. W. Heath, N. González-Prelcic, S. Rangan, W. Roh, and A. M. Sayeed, "An overview of signal processing techniques for millimeter wave MIMO systems," *IEEE J. Sel. Topics Signal Process.*, vol. 10, no. 3, pp. 436–453, Apr. 2016.

[37] *NR; Physical Layer Procedures for Data (Release 18)*, document TS 38.214, Version 18.1.0, 3GPP, 2024.

[38] *IEEE Standard for Information Technology–Telecommunications and Information Exchange Between Systems–Local and Metropolitan Area Networks–Specific Requirements—Part 11: Wireless LAN Medium Access Control (MAC) and Physical Layer (PHY) Specifications Amendment 3: Enhancements for Very High Throughput in the 60 GHz Band*, Standard IEEE 802.11ad—2012, 2012.

[39] *IEEE Standard for Information Technology–Telecommunications and Information Exchange Between Systems Local and Metropolitan Area Networks–Specific Requirements—Part 11: Wireless LAN Medium Access Control (MAC) and Physical Layer (PHY) Specifications Amendment 2: Enhanced Throughput for Operation in License-exempt Bands Above 45 GHz*, Standard IEEE 802.11ay—2021, 2021.

[40] K. M. Braun, "OFDM radar algorithms in mobile communication networks," Ph.D. dissertation, Karlsruher Inst. Für Technologie (KIT), Karlsruhe, Germany, 2014.

[41] X. Gu, D. Liu, C. Baks, O. Tageman, B. Sadhu, J. Hallin, L. Rexberg, P. Parida, Y. Kwark, and A. Valdes-Garcia, "Development, implementation, and characterization of a 64-element dual-polarized phased-array antenna module for 28-GHz high-speed data communications," *IEEE Trans. Microw. Theory Techn.*, vol. 67, no. 7, pp. 2975–2984, Jul. 2019.

[42] D. Guermandi, Q. Shi, A. Dewilde, V. Derudder, U. Ahmad, A. Spagnolo, I. Ocket, A. Bourdoux, P. Wambacq, J. Craninckx, and W. Van Thillo, "A 79-GHz 2 × 2 MIMO PMCW radar SoC in 28-nm CMOS," *IEEE J. Solid-State Circuits*, vol. 52, no. 10, pp. 2613–2626, Oct. 2017.

[43] M. Richards, *Principles of Modern Radar*. Stevenage, U.K.: Institution of Engineering and Technology, 2014.

[44] S. Khosravi, H. Shokri-Ghadikolaei, and M. Petrova, "Learning-based handover in mobile millimeter-wave networks," *IEEE Trans. Cognit. Commun. Netw.*, vol. 7, no. 2, pp. 663–674, Jun. 2021.

[45] R. W. Bohannon and A. Williams Andrews, "Normal walking speed: A descriptive meta-analysis," *Physiotherapy*, vol. 97, no. 3, pp. 182–189, Sep. 2011.
[46] C. Van Loan, *Computational Frameworks for the Fast Fourier Transform*. Philadelphia, PA, USA: Society for Industrial and Applied Mathematics, 1992.

RIZQI HERSYANDIKA (Graduate Student Member, IEEE) received the B.Eng. degree in telecommunication engineering from Bandung Institute of Technology, Indonesia, in 2010, and the M.Sc. degree in electrical engineering from Delft University of Technology, The Netherlands, in 2016. He is currently pursuing the Ph.D. degree with the WaveCoRE Arenberg Group, Department of Electrical Engineering (ESAT), KU Leuven, Belgium, and part of the H2020-MSCA-ITN MINTS Project. He also had working experience as a Spectrum Monitoring Engineer with the Ministry of Communication and IT, Indonesia. His research interests include mmWave communication, cell-free networks, spectrum management, and integrated sensing and communication.

ADHAM SAKHNINI (Student Member, IEEE) received the M.Sc. degree in engineering mathematics from Lund University, Sweden, in 2020. He is currently pursuing the Ph.D. degree in electrical engineering with the Interuniversity Microelectronics Centre (IMEC) and Katholieke Universiteit Leuven (KU Leuven), Belgium. His research interests include the analysis and design of radar and communication systems, signal processing with applications in detection and estimation, interference mitigation, synchronization, and performance analysis.

YANG MIAO (Senior Member, IEEE) received the M.Sc. and Ph.D. degrees from the Radio Propagation Laboratory, Mobile Communications Research Group, Tokyo Institute of Technology, Tokyo, Japan, in 2012 and 2015, respectively. From 2010 to 2015, she was a Research Assistant with the Takada Laboratory, Tokyo Institute of Technology. From 2015 to 2018, she was a Postdoctoral Researcher with the Institute of Information and Communication Technologies, Electronics, and Applied Mathematics, Universite Catholique de Louvain, Louvain-la-Neuve, Belgium, and IMEC, Wireless, Acoustics, Environment, and the Expert Systems Laboratory, Ghent University, Ghent, Belgium. From 2017 to 2018, she was a part-time Senior Antenna Engineer with Jaguar Radio Wave Corporation, Shenzhen, China. From 2018 to 2019, she was a Research Assistant Professor with the Southern University of Science and Technology, Shenzhen. From August 2019 to May 2024, she was an Assistant Professor with the Radio Systems Group, University of Twente, 4TU, The Netherlands, where she has been an Associate Professor, since June 2024. Since November 2021, she has also been affiliated part-time with KU Leuven, Leuven, Belgium, as a Marie Curie Individual Fellow. Her research interests include joint communication and sensing, incorporating mobility, and human factors. She is a Senior Member of URSI.

QING WANG (Senior Member, IEEE) received the Ph.D. degree from the UC3M and IMDEA Networks Institute, Spain, in 2016. He is currently an Assistant Professor with the Embedded Systems Group, Delft University of Technology, The Netherlands. His research interests include visible light communication and sensing and embedded AI/TinyML for the IoT and 6G. He is the Co-Founder of OpenVLC, an open-source and low-cost platform for VLC research. His research outcomes have been published at IEEE/ACM conferences and journals, such as MobiCom, CoNEXT, SenSys, MobiSys, and ICLR. He has received nine paper awards, including the Best Paper Awards from WoWMoM'24, ICC'23, EWSN'23, SenSys'22, Morse'22, and COMSNETS'19; and the Best Paper Runner-Up Awards from EWSN'22, MobiCom'20 (Honourable Mention), and CoNEXT'16.

SOFIE POLLIN (Senior Member, IEEE) is currently a Professor with KU Leuven, focusing on wireless communication systems. Before that, she worked with IMEC and the University of California at Berkeley. She is also a Principal Member of the Technical Staff with IMEC. Her research interests include wireless networks that require networks that are ever more dense, heterogeneous, battery-powered, spectrum-constrained, cell-free networks, integrated communication and sensing, and non-terrestrial networks.